nature photonics

ARTICLES

PUBLISHED ONLINE: 13 OCTOBER 2013 | DOI: 10.1038/NPHOTON.2013.256

Experimental realization of an epsilon-near-zero metamaterial at visible wavelengths

Ruben Maas[1]*, James Parsons[1], Nader Engheta[2] and Albert Polman[1]

Optical materials with a dielectric constant near zero have the unique property that light advances with almost no phase advance. Although such materials have been made artificially in the microwave and far-infrared spectral range, bulk three-dimensional epsilon-near-zero (ENZ) engineered materials in the visible spectral range have been elusive. Here, we present an optical metamaterial composed of a carefully sculpted parallel array of subwavelength silver and silicon nitride nanolamellae that shows a vanishing effective permittivity, as demonstrated by interferometry. Good impedance matching and high optical transmission are demonstrated. The ENZ condition can be tuned over the entire visible spectral range by varying the geometry, and may enable novel micro/nanooptical components, for example, transmission enhancement, wavefront shaping, controlled spontaneous emission and superradiance.

Optical metamaterials have been the topic of intense study in recent years because they enable the realization of optical properties that do not occur in natural materials. Metamaterials are composed of elements with subwavelength scales in one or more dimensions. For this reason, metamaterials have been studied in the microwave spectral range, where index-near-zero[1] and epsilon-near-zero (ENZ) behaviours have been predicted theoretically[2–4] and demonstrated experimentally[5–10]. With the appearance of advanced ion- and electron-beam nanolithography methods, the realization of ENZ metamaterials in the visible spectral range has now come within reach. Recently, a one-dimensional waveguide nanochannel with ENZ behaviour was demonstrated in the visible[11]. If three-dimensional ENZ metamaterials could be made in the visible, entirely new forms of waveform shaping[3,12], light tunnelling[4] and spontaneous emission enhancement[13] would become possible over this technologically important spectral range.

Here, we present a metamaterial design composed of alternating layers of Ag and SiN with subwavelength layer thicknesses (Fig. 1a, inset). This geometry has been studied previously to construct hyperbolic wavevector diagrams and increase the photonic density of states[14–18]. In the limit of deep subwavelength layer thicknesses, and for transverse electric (TE) polarized light (that is, the electric field parallel to the waveguides), the effective permittivity of this metamaterial equals the geometrically averaged permittivity[18], $\varepsilon_{av} = \rho\varepsilon_m + (1-\rho)\varepsilon_d$, where ρ is the metal filling fraction and ε_m and ε_d are the permittivity of metal and dielectric, respectively. Figure 1a shows experimentally determined values of the real (ε', solid lines) and imaginary (ε'', dashed lines) values of the permittivity for a thin Ag layer. The plot for ε' demonstrates the well-known decreasing trend towards strongly negative values due to the Drude-type response of free electrons in metal at long wavelengths. The effective permittivity of SiN is also shown in the figure and is positive and only slightly dispersive. The imaginary part of the permittivity of both Ag and SiN is measured to be very small over the entire visible range. (Supplementary section 'Ellipsometry'.)

Figure 1b shows the calculated effective permittivity for TE polarized light for a metamaterial composed of deep subwavelength Ag and SiN layers with $\rho = 20$, 30 and 50%, based on the optical constants in Fig. 1a. With these metal filling fractions, the ENZ condition occurs at $\lambda = 662$, 545 and 428 nm, respectively, demonstrating the ENZ condition can be controlled over a broad spectral range by varying the composition. At the same time, the imaginary part of the effective permittivity ε'' is close to zero (<0.2) over the entire visible range, indicating low loss.

The permeability of the metamaterial is assumed to be unity throughout the entire visible spectrum, as there is no magnetic resonance in the system. This means that when $\varepsilon' = 1$ the metamaterial is completely matched to free space, and almost no light would be reflected. Figure 1b shows that the wavelength at which this condition is met can be tuned throughout the visible range by varying ρ. As an example, for $\rho = 30\%$ we find $\varepsilon' = 1$ at $\lambda = 491$ nm. Interestingly, the losses are relatively low in this case ($\varepsilon'' < 0.1$), even though a significant portion of the metamaterial consists of metal, and the optical frequency is quite close to the bulk plasma frequency of the metal.

Probing the ENZ condition on this layered metamaterial requires samples that are optically accessible along the planar layers (x-direction), which cannot be achieved using geometries made by thin-film evaporation. Here, we demonstrate a layered metamaterial architecture composed of vertically oriented parallel lamellae of Ag and SiN, fabricated from a SiN membrane using a combination of focused ion beam (FIB) milling, reactive ion etching and thermal evaporation of Ag. This configuration allows us to isolate the ENZ condition using TE polarized light. Note that TE and transverse magnetic (TM) polarized light are degenerate when incident normal to the layers. Moreover, in the latter geometry, higher-order Bloch harmonics can complicate the analysis. Figure 2a shows a top-view scanning electron micrograph (SEM) of a completed metamaterial sample (see Supplementary section 'Fabrication', for more details). The 8 μm × 8 μm waveguide arrays are highly regular, and the Ag and SiN layers are clearly visible as bright and dark bands, with layer thicknesses of 110 nm and 130 nm, respectively. A cross-section of the metamaterial structure is shown in Fig. 2b. The metamaterial layer can be clearly seen, on top of a remaining underlayer of SiN.

A total of 16 different multilayered metamaterial samples were fabricated. The exact waveguide dimensions, metamaterial thickness

[1]Center for Nanophotonics, FOM Institute AMOLF, Science Park 104, 1098 XG, Amsterdam, The Netherlands, [2]Department of Electrical and Systems Engineering, University of Pennsylvania, 200 South 33rd Street, Philadelphia, Pennsylvania 19104-6314, USA. *e-mail: maas@amolf.nl

© 2013 Macmillan Publishers Limited. All rights reserved.

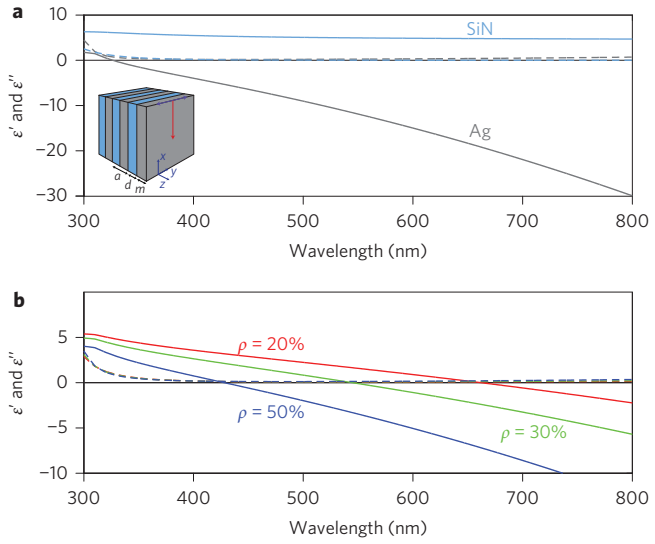

Figure 1 | Metamaterial optical constants. a, Measured real (ε', solid line) and imaginary (ε'', dashed line) permittivity of Ag (grey) and SiN (blue). Inset: schematic of the multilayered metamaterial structure composed of Ag and SiN layers (*a*, *d* and *m* are unit cell dimension and dielectric and metal layer thicknesses, respectively). Light is incident along the *x*-direction and polarized along the *y*-direction. The dashed lines for Ag and SiN coincide. **b**, Effective permittivity of an Ag/SiN multilayered metamaterial with metal filling fraction $\rho = 20\%$ (red), 30% (green) and 50% (blue), calculated using an effective medium approximation. The real (ε', solid lines) and imaginary (ε'', dashed lines) parts of the permittivity are shown. The dashed lines for the three filling fractions coincide.

and underlayer thickness of each sample were determined from cross-sections made using FIB. The metal layer thickness was varied from 40 to 150 nm, and the dielectric layer thickness between 36 and 135 nm. In this way, the metal filling fraction ρ was systematically varied between 30 and 80% to study its effect on metamaterial dispersion. The unit cell size was varied between 85 and 280 nm to investigate the transition from an effective medium material to that of a waveguide-based metamaterial.

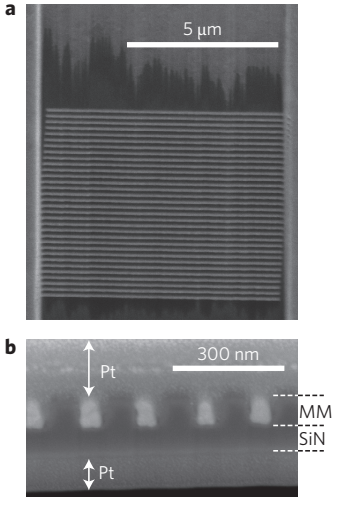

Figure 2 | Metamaterial sample. a, SEM top view of the completed metamaterial structure. The Ag and SiN layers are visible as bright and dark bands, with layer thicknesses of 110 nm and 130 nm, respectively. **b**, SEM view of a cross-section showing the metamaterial (MM) layer, with alternating layers of Ag (bright) and SiN (dark), as well as a continuous SiN layer under the metamaterial. Pt layers are deposited to emphasize the top and bottom interface.

Interferometric phase measurements

To determine the effective optical properties of each multilayered metamaterial, we used a specially designed Mach–Zehnder interferometer to measure the optical path length of the metamaterial structures[19] (Supplementary section 'Interferometry'). The optical path length was determined from the difference between the phase of light focused through the metamaterial and light focused through an air reference hole made in the same sample.

Figure 3a shows the measured phase shifts for metamaterials composed of a unit cell of a thin metal layer (40, 58 nm) in combination with a thin (45 nm, blue) and thick (135 nm, red) dielectric layer, respectively. Figure 3b shows similar data for a thick metal layer (155 nm, 150 nm) in combination with thin (36 nm, blue) and thick (130 nm, red) dielectric layers. The experimental data, taken at seven different wavelengths, show a gradual transition from a large phase shift at short wavelengths to a small phase shift at longer wavelengths.

Figure 3 (solid lines) also shows finite-difference time-domain simulations (FDTD Solutions 8.0, Lumerical Solutions) of the phase shift as a function of wavelength. In these simulations, the metamaterial waveguide dimensions determined from cross-sections are used to define a periodic unit cell, and the experimentally determined optical constants of Ag and SiN (Fig. 1a) are used, so no fitting parameters are applied. Figure 3 shows very good agreement between experiment and simulations for all four samples. The gradual decrease in phase shift for longer wavelengths is clearly reproduced by the simulations. Also, the distinct feature in the data around $\lambda = 480$ nm for the largest unit cell in Fig. 3b is well reproduced. Its origin will be discussed in the following.

To determine the effective permittivity of the metamaterial from the measured phase shift, a transfer matrix method was applied to a double-layer structure composed of the metamaterial sample and the SiN underlayer, surrounded by air. This model expresses the effective complex transmission coefficient t_{eff} of the combined metamaterial and underlayer structure in terms of their respective thickness and (effective) permittivity. The phase shift of light transmitted through the metamaterial relative to that through the

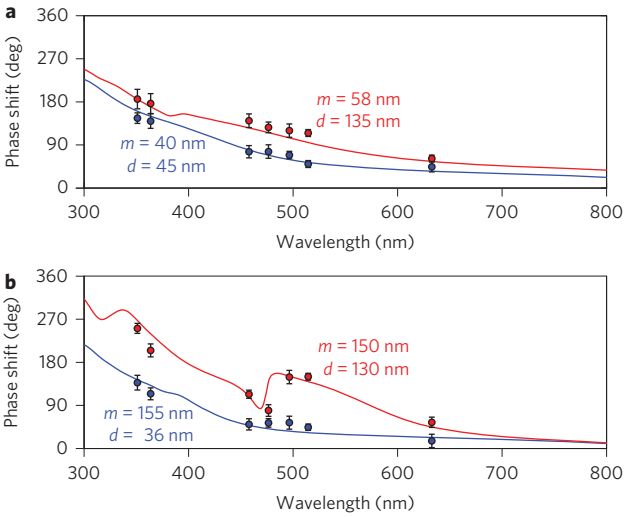

Figure 3 | Metamaterial phase measurements. Measured (data points) and simulated (solid lines) phase shift of metamaterials with different metal (*m*) and dielectric (*d*) layer thicknesses. **a**, Thin metal layer and varying dielectric thickness. **b**, Thick metal layer and varying dielectric thickness. Error bars correspond to the standard deviation of the collection of 20 consecutive phase measurements.

© 2013 Macmillan Publishers Limited. All rights reserved.

reference hole $\Delta\phi = \phi_s - \phi_r$ directly follows using $\phi_s = \arg(t_{eff})$ and $\phi_r = k_0(d_s + d_{SiN})$, where k_0, d_s and d_{SiN} are the free-space wavevector, the thickness of the metamaterial sample and the thickness of the SiN underlayer, respectively. From the measured phase shift, the known thickness of metamaterial and SiN underlayer and the known permittivity of SiN, the effective permittivity of the metamaterial can be derived. This procedure is illustrated by the inset in Fig. 4a, which shows the phase shift calculated as described above for a metamaterial sample ($d_s = 45$ nm; $d_{SiN} = 93$ nm, in blue) at $\lambda = 633$ nm as a function of metamaterial permittivity. The imaginary part of the effective permittivity is assumed to be $\varepsilon'' = 0$. The validity of this assumption is discussed in the Supplementary section 'Effective permittivity'. Also shown in the inset is the measured phase shift for this geometry (horizontal red line). The effective permittivity then directly follows from the intersection between the two lines. The phase shift was measured 20 times for each metamaterial sample at each wavelength, and every measured phase shift was separately converted to an effective permittivity. The mean of this distribution was taken to be the effective permittivity of the sample, with the standard deviation of the distribution an indicator for the error. For metamaterial thicknesses greater than 15 nm, using simulations, we verified that the effective permittivity is independent of thickness (Supplementary section 'Thickness dependence').

Changing effective parameters

Figure 4a shows the effective permittivity derived in this way for three different metamaterials, with each structure having the same unit cell size of ~200 nm, and the metal filling fraction varied ($\rho = 30$, 60 and 80%). For all filling fractions a clear trend of decreasing permittivity with wavelength is observed. The measured permittivity ranges from $\varepsilon' = 6.0 \pm 1.2$ at $\lambda = 364$ nm for the lowest filling fraction to $\varepsilon' = -13 \pm 3.4$ at $\lambda = 633$ nm for the highest filling fraction. Figure 4a also shows analytical calculations of the metamaterial effective permittivity (solid lines). This effective permittivity is determined by calculating the supported eigenmodes of a planar waveguide array using a transfer matrix formalism for a periodic unit cell[20,21]. The eigenmodes are calculated assuming light propagation parallel to the waveguides, with the electric field parallel to the metal–dielectric interfaces (TE polarization). Only the fundamental mode (characterized by the lowest propagation losses) is assumed to contribute to wave propagation through the metamaterial. The calculations are in good agreement with the experimental trends. The strong difference in dispersion between the three geometries is also well represented by the calculations, confirming that the wavelength at which the effective permittivity of the metamaterial becomes zero can be controlled by the metal filling fraction. This cutoff condition occurs at $\lambda = 807$, 567 and 394 nm for the three geometries, respectively.

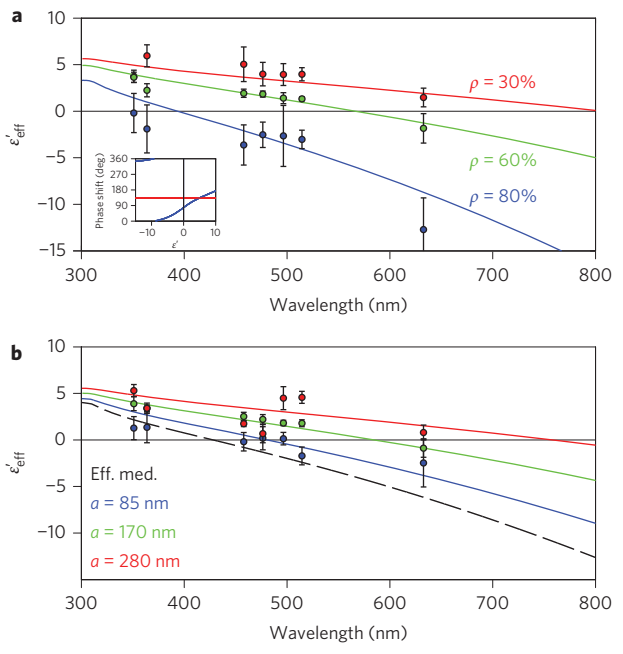

Figure 4 | Metamaterial effective permittivity. a, Measured (data points) and calculated (solid lines) effective permittivity for 200 nm unit cell structures with metal filling fraction $\rho = 30\%$ (red), 60% (green) and 80% (blue). Inset: calculated phase shift (solid lines) as a function of effective metamaterial permittivity for a metamaterial sample ($d_s = 45$ nm; $d_{SiN} = 93$ nm, in blue) at $\lambda = 633$ nm. The measured phase shift is indicated by the horizontal red line. **b**, Measured and calculated effective permittivity for structures with a metal filling fraction of $\rho = 50\%$ and different unit cell size $a = 280$ nm (red), 170 nm (green) and 85 nm (blue). The effective permittivity based on the geometric average is also shown as the black dashed line. Error bars correspond to the standard deviation of the measured phase shifts converted to effective permittivity.

Figure 4b shows the measured and calculated effective permittivity of three structures with an approximately constant metal filling fraction $\rho = 50\%$. Here, the unit cell size is varied ($a = 85$, 170 and 280 nm). The experimental trends are well reproduced by the calculations for the 85 and 170 nm layer thicknesses. For the 280 nm layer thickness, differences are observed between calculations and experiment that are attributed to the excitation of higher-order waveguide modes that are not included in the calculation. This aspect will be discussed shortly. The black dashed curve in Fig. 4b shows the geometrically averaged permittivity ε_{av}, calculated based on the effective medium theory assuming $\rho = 50\%$. Clearly, the experimental data and the results of the analytical calculation are strongly redshifted compared to this simple model. Indeed, in our metamaterial geometry, with metal thicknesses larger than the skin depth, the electric field is partially excluded from the metal region, causing the effective medium approximation to be invalid. Because of this exclusion, the metal filling fraction is effectively lowered, resulting in a redshift. The data in Fig. 4 show how the ENZ condition can be controlled through the 400–800 nm spectral range for any given unit cell size by an appropriately chosen metal filling fraction.

To further study the metamaterial dispersion, we measured the transmission spectra for each metamaterial structure. Data were taken using a white-light source and a spectrograph equipped with a charge-coupled device (CCD) detector, and the spectra were normalized to the transmission through a reference hole. Figure 5a–d shows the transmission spectra for the four structures represented in Fig. 3. In all cases, the transmission is highly wavelength dependent; the transmission peaks at a value as high as 90% for the 58 nm Ag/135 nm SiN metamaterial. Figure 5 also shows the simulated transmission (solid green lines) for the measured waveguide dimensions, taking into account the SiN underlayer. Overall, the experimental peak wavelengths are well reproduced by the simulation. The lower transmission for the 155 nm Ag/36 nm SiN metamaterial is also reproduced in the calculations. We attribute the difference in spectral shape between measurement and simulation to variations in waveguide dimensions across the sample. The reduced signal-to-noise ratio observed for wavelengths below 400 nm is caused by the low sensitivity of the CCD detector in this regime.

To explain the origin of the transmission maximum, we also simulated the transmission of the same metamaterial geometries, but now without the SiN underlayer (dashed green lines). Also indicated in Fig. 5 are the wavelengths at which the calculated effective permittivity of the metamaterial equals 1 (vertical grey dashed lines). In all cases, the wavelength at which $\varepsilon' = 1$ agrees well with

© 2013 Macmillan Publishers Limited. All rights reserved.

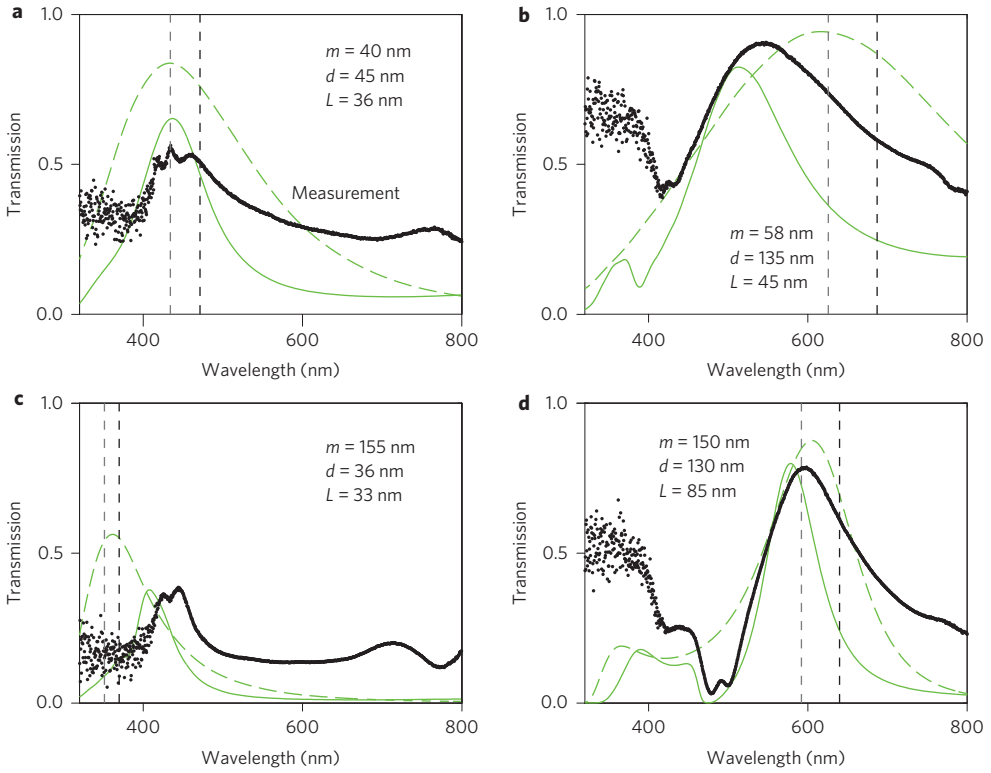

Figure 5 | Transmission spectra and matching condition. Measured (black) and simulated (solid green) transmission spectra for four different metamaterial structures. The simulated transmission without the SiN underlayer (dashed green line) peaks at the same wavelength where the effective permittivity of the structure is around 1 (vertical grey dashed line), corresponding to air. The wavelength at which the effective permittivity is near zero is indicated by the vertical black dashed line.

the wavelength of the peak in transmission (when there is no SiN underlayer), indicating that the transmission maximum results from a matched effective permittivity of the metamaterial to the surrounding air. The measured transmission peaks occur at slightly blueshifted wavelengths because, with the SiN underlayer present, the metamaterial sample effectively acts as an antireflection coating for the SiN underlayer. Indeed, such optimum impedance matching occurs for a metamaterial permittivity between that of air and SiN, which is in the blueshifted spectral range.

The vertical black dashed lines in Fig. 5 indicate the wavelengths at which the metamaterials reach the ENZ condition. The calculated transmission for the case without the SiN underlayer is still very high (for example, $T = 87\%$ in Fig. 5b), although somewhat reduced compared to the transmission at the impedance-matched $\varepsilon' = 1$ condition wavelength. This is caused by an increased impedance mismatch and a reduced propagation length (Supplementary section 'Propagation length'), leading to both increased reflection and increased absorption.

Size and angular dependence

An important criterion for metamaterials is that the constituent elements are subwavelength. Therefore, it is interesting to study how the effective optical properties change with unit cell size. As Fig. 4b demonstrates, a distinct redshift of the dispersion is observed for larger unit cell sizes with the same filling fraction. To further quantify this effect we calculated the supported waveguide eigenmode for different unit cell sizes. Figure 6a shows the calculated effective mode index using the same transfer matrix method described above, for a periodic unit cell with a constant metal filling fraction of 30%, and a unit cell size ranging from $a = 1$ nm to 600 nm at a free-space wavelength of $\lambda = 515$ nm. As can be seen, the real part of the mode index of the fundamental mode (solid black line) clearly converges to the expected index based on the effective-medium theory (dashed green line) for small unit cell dimensions ($n'_{\mathrm{eff}} = 0.75$ for this geometry). For large unit cell dimensions, the mode index approaches the SiN index (dashed blue line), as most of the light is excluded from the thick metal layers. The same behaviour is observed for the imaginary part of the index, as can be seen in Fig. 6b.

Around a unit cell size of $a = 250$ nm, the first higher-order waveguide mode is no longer cut off at $\lambda = 515$ nm. The effective index for this mode is also shown in Fig. 6a as the solid grey line. Figure 6b shows that, for a unit cell larger than 300 nm, the imaginary part of this mode becomes comparable to that of the fundamental waveguide mode. The presence of higher-order modes limits the maximum unit cell dimensions allowed in the design of this metamaterial. Interestingly, the first higher-order mode was in fact observed in the measured and simulated phase shift for the largest fabricated unit cell ($a = 280$ nm), as can be seen in Fig. 3b. The distinct oscillatory feature observed around 480 nm is due to a transition between the fundamental and the first higher-order mode.

So far, we have considered normally incident light. Next, we address the response of our three-dimensional ENZ metamaterial in the angular range between parallel incidence (along x) and perpendicular incidence (along z). Figure 6c shows the calculated wavevector diagram for light in the x–z plane (free-space wavelength $\lambda = 460$ nm), for $a = 85$ nm and $\rho = 47\%$. To determine the response of the metamaterial for all incident angles, we performed two different calculations[21]. The first calculation determines the fundamental waveguide mode for a given small ($k_z < k_0$), real-valued k_z component (shown in blue). This calculation determines the wave propagation for light mainly along x. The second calculation determines the fundamental Bloch wavevector, assuming a small real-valued wavevector component along x ($k_x < k_0$) (shown in red).

© 2013 Macmillan Publishers Limited. All rights reserved.

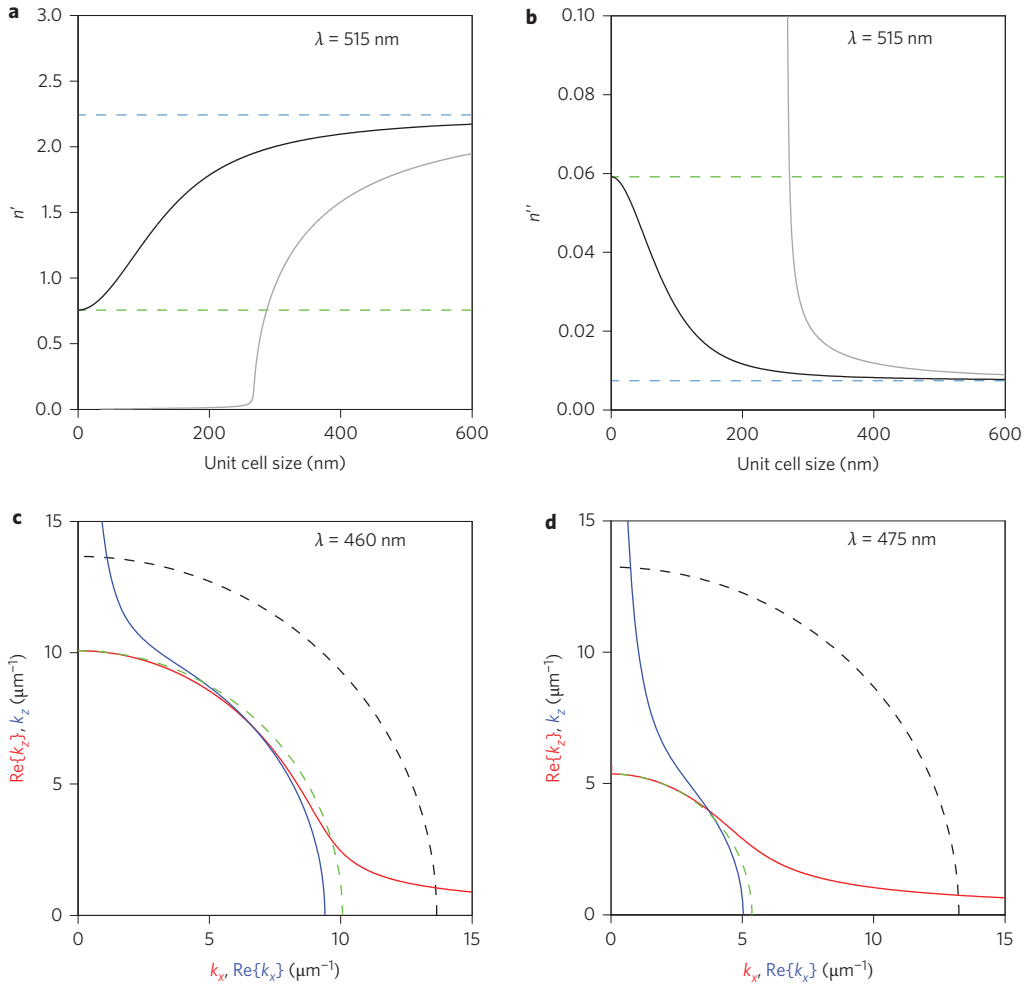

Figure 6 | Isotropic index. a,**b**, Real (**a**) and imaginary (**b**) part of the mode index of the fundamental TE waveguide mode (black) and the first higher-order mode (grey) calculated versus unit cell size. For small unit cell sizes the effective index approaches the geometrically averaged index (green dashed lines), and for large unit cell sizes the mode index approaches the refractive index of SiN (blue dashed lines). **c**, Wavevector diagram for $\lambda = 460$ nm ($a = 85$ nm, $\rho = 47\%$), demonstrating an effective index that is independent of angle. The green dashed curve corresponds to the expected isotropic index, and the black dashed curve is the wavevector in free space. **d**, Wavevector diagram calculated for $\lambda = 475$ nm. The mode index is reduced and still angle independent.

This situation represents wave propagation mainly along z. Also shown is the wavevector diagram of light propagation in air (black dashed line), and light propagation with an isotropic index equal to the waveguide mode index when $k_z = 0$ (green dashed line). The fact that the calculated wavevector diagram follows the isotropic index in their respective regions of interest indicates that for a unit cell of $a = 85$ nm the effective index of the structure is nearly angle independent. A small unit cell is required to obtain an angle independent refractive index, as light propagation normal to the waveguide interfaces (along z) is described by a Bloch wave composed of a series of harmonics, separated by the reciprocal lattice constant $\Lambda = 2\pi/a$ (ref. 20): Λ must then remain much larger than wavevector k_z.

Figure 6d shows a wavevector diagram at a free-space wavelength of $\lambda = 475$ nm. Here, the mode index is strongly reduced because the metamaterial approaches cutoff, yet the response is still angle independent. When the mode index further approaches zero, the wavevector diagram will no longer be spherical, and the calculated value of k_x (k_z) will become independent of the k_z (k_x) component.

Conclusions

In conclusion, we have designed, fabricated and characterized an optical multilayered metamaterial consisting of thin Ag and SiN layers with an effective permittivity in the visible spectrum ranging from $\varepsilon' = 6.0 \pm 1.2$ to $\varepsilon' = -13 \pm 3.4$. The metamaterial is highly dispersive through the $\lambda = 400$–800 nm spectral range, and the dispersion is determined by the layer thicknesses and relative filling fraction. The epsilon-near-zero condition is experimentally demonstrated at wavelengths in the range $\lambda = 351$–633 nm. The optical transmission of the metamaterial is as high as 90%, and impedance matching to air is observed when $\varepsilon' = 1$. The experimental data correspond well with analytical calculations and simulations. The transition from an effective medium material for small unit cell size to that of a coupled waveguide material for larger dimensions is studied. For unit cell size $a = 85$ nm, calculations show that the effective index is independent of angle. This highly dispersive metamaterial may find applications in transmission enhancement, wavefront shaping, control of spontaneous emission and superradiance.

Methods

Metamaterial samples were fabricated from a SiN membrane. The waveguide pattern was written in a Cr masking layer (20 nm) using FIB milling at normal incidence. The pattern was transferred to the SiN using an anisotropic CHF_3/O_2 reactive ion etch recipe. The etched channels were in-filled with Ag using physical vapour deposition. The surface of the metamaterial was then polished using FIB milling at oblique incidence.

The optical path length of the metamaterial sample was measured in a Mach–Zehnder interferometer. Light was focused through the metamaterial, and the length

© 2013 Macmillan Publishers Limited. All rights reserved.

of the reference arm was changed with a piezo-electrically driven mirror, causing a sinusoidally oscillating intensity at the output. Light was then focused through a reference hole in the membrane, and the same reference mirror movement was performed. The sinusoidal signal was now displaced by a phase shift, caused by the optical path length of the metamaterial sample.

The simulated phase shift was obtained from FDTD simulations (Lumerical). We recorded the phase and amplitude of the transmitted plane wave after propagation through the structure. First the structure consisted only of a single SiN layer. The thickness of this SiN layer was increased from zero to the realized thickness, in steps of 1 nm. The thickness of the metamaterial on top of the SiN layer was then increased to the fabricated thickness.

Received 24 April 2013; accepted 3 September 2013; published online 13 October 2013

References

1. Ziolkowski, R. W. Propagation in and scattering from a matched metamaterial having a zero index of refraction. *Phys. Rev. E* **70,** 046608 (2004).
2. Silveirinha, M. & Engheta, N. Tunneling of electromagnetic energy through subwavelength channels and bends using epsilon-near-zero materials. *Phys. Rev. Lett.* **97,** 157403 (2006).
3. Alù, A., Silveirinha, M., Salandrino, A. & Engheta, N. Epsilon-near-zero metamaterials and electromagnetic sources: tailoring the radiation phase pattern. *Phys. Rev. B* **75,** 155410 (2007).
4. Alù, A. & Engheta, N. Light squeezing through arbitrarily shaped plasmonic channels and sharp bends. *Phys. Rev. B* **78,** 035440 (2008).
5. Edwards, B., Alù, A., Young, M., Silveirinha, M. & Engheta, N. Experimental verification of epsilon-near-zero metamaterial coupling and energy squeezing using a microwave waveguide. *Phys. Rev. Lett.* **100,** 033903 (2008).
6. Edwards, B., Alù, A., Silveirinha, M. & Engheta, N. Reflectionless sharp bends and corners in waveguides using epsilon-near-zero effects. *J. Appl. Phys.* **105,** 044905 (2009).
7. Adams, D. *et al.* Funneling light through a subwavelength aperture with epsilon-near-zero materials. *Phys. Rev. Lett.* **107,** 133901 (2011).
8. Rizza, C., Di Falco, A. & Ciattoni, A. Gain assisted nanocomposite multilayers with near zero permittivity modulus at visible frequencies. *Appl. Phys. Lett.* **99,** 221107 (2011).
9. Vassant, S. *et al.* Epsilon-near-zero mode for active optoelectronic devices. *Phys. Rev. Lett.* **109,** 237401 (2012).
10. Liu, R. *et al.* Experimental demonstration of electromagnetic tunneling through an epsilon-near-zero metamaterial at microwave frequencies. *Phys. Rev. Lett.* **100,** 023903 (2008).
11. Vesseur, E. J. R., Coenen, T., Caglayan, H., Engheta, N. & Polman, A. Experimental verification of $n = 0$ structures for visible light. *Phys. Rev. Lett.* **110,** 013902 (2013).
12. Luo, J., Xu, P. & Gao, L. Directive emission based on one-dimensional metal heterostructures. *J. Opt. Soc. Am. B* **29,** 35–39 (2012).
13. Alù, A. & Engheta, N. Boosting molecular fluorescence with a plasmonic nanolauncher. *Phys. Rev. Lett.* **103,** 043902 (2009).
14. Naik, G. V., Liu, L., Kildishev, A. V., Shalaev, V. M. & Boltasseva, A. Demonstration of Al:ZnO as a plasmonic component for near-infrared metamaterials. *Proc. Natl Acad. Sci. USA* **109,** 8834–8838 (2012).
15. Krishnamoorthy, H. N. S., Jacob, Z., Narimanov, E. E., Kretzschmar, I. & Menon, V. M. Topological transitions in metamaterials. *Science* **336,** 205–209 (2012).
16. Jacob, Z. *et al.* Engineering photonic density of states using metamaterials. *Appl. Phys. B* **100,** 215–218 (2010).
17. Jacob, Z. & Shalaev, V. M. Plasmonics goes quantum. *Science* **334,** 463–464 (2011).
18. Cortes, C. L., Newman, W., Molesky, S. & Jacob, Z. Quantum nanophotonics using hyperbolic metamaterials. *J. Opt.* **14,** 063001 (2012).
19. Dolling, G., Enkrich, C., Wegener, M., Soukoulis, C. M. & Linden, S. Simultaneous negative phase and group velocity of light in a metamaterial. *Science* **312,** 892–894 (2006).
20. Russel, P. St. J., Briks, T. A. & Lloyd-Lucas, F. D. in *Confined Electrons and Photons* (eds Burstein, E. & Weisbuch, C.) 585–633 (Plenum, 1995).
21. Verhagen, E., de Waele, R., Kuipers, L. & Polman, A. Three-dimensional negative index of refraction at optical frequencies by coupling plasmonic waveguides. *Phys. Rev. Lett.* **105,** 223901 (2010).

Acknowledgements

This work is part of the research programme of the Foundation for Fundamental Research on Matter (FOM), which is financially supported by The Netherlands Organization for Scientific Research (NWO). It is also funded by the European Research Council. N.E. acknowledges support from the US Air Force Office of Scientific Research (AFOSR) Multidisciplinary University Research Initiative (MURI; grant no. FA-9550-12-1-0488).

Author contributions

N.E. and A.P. conceived the idea and designed the experiment. J.P. designed and constructed the interferometer. R.M. fabricated the sample, carried out the interferometric and optical transmission measurements, and performed calculations and numerical modelling. All authors contributed to analysing the experimental data and writing the manuscript.

Additional information

Supplementary information is available in the online version of the paper. Reprints and permissions information is available online at www.nature.com/reprints. Correspondence and requests for materials should be addressed to R.M.

Competing financial interests

The authors declare no competing financial interests.

© 2013 Macmillan Publishers Limited. All rights reserved.